Please cite this paper as:

Li JY, Zhu S, Shi X, and Shen W (2022). Electromagnetic Shunt Damper for Bridge Cable Vibration Mitigation: Full-Scale Experimental Study. *Journal of Structural Engineering* 146: 04019175.

https://doi.org/10.1061/(ASCE)ST.1943-541X.0002477

# Electromagnetic Shunt Damper for Bridge Cable Vibration Mitigation: a Full-scale Experimental Study

Jin-Yang Li[1], Songye Zhu[2,] *, Xiang Shi[3], Wenai Shen[4]

1. Department of Civil and Environmental Engineering, The Hong Kong Polytechnic University, Hung Hom, Kowloon, Hong Kong, China
2. Department of Civil and Environmental Engineering, and The Hong Kong Branch of National Rail Transit Electrification and Automation Engineering Technology Research Center, The Hong Kong Polytechnic University, Hung Hom, Kowloon, Hong Kong, China
3. College of Information and Control Engineering, China University of Petroleum (East China), Qingdao 266580, Shandong Province, China
4. School of Civil Engineering and Mechanics, Huazhong University of Science and Technology, Wuhan 430074, Hubei Province, China

* Corresponding author: Dr. Songye Zhu, Email: songye.zhu@polyu.edu.hk

**ABSTRACT:**

Long bridge cables are vulnerable to unanticipated large vibrations induced by earthquakes, wind, and traffic loads. The use of various dampers, including inerter dampers (IDs), as an effective approach for the mitigation of cable vibration has been extensively studied in recent years. This work presents an innovative strategy wherein an electromagnetic shunt damper (EMSD) is applied to emulate the mechanical behaviors of traditional IDs. The proposed EMSD–ID design exploits analogous relationships between mechanical and electrical systems and provides unprecedented efficiency and flexibility in exerting large inertance. A full-scale EMSD–ID prototype was designed and fabricated, and its effective control performance was verified in a laboratory experiment involving a cable-stayed bridge model with a length of 135 m.

## 1. Introduction

Over the past several years, numerous systematic studies have focused on the use of supplemental energy-dissipating dampers to suppress the excessive vibrations of stay cables given its small inherent damping. A popular conclusion reached by these studies is that the maximum damping ratio that can be added to stay cables by a passive linear viscous damper is capped by approximately one half of the ratio of the distance from the cable anchorage to the damper over the entire cable length (Krenk 2000; Xu and Yu 1998; Main and Jones 2002; Krenk and Høgsberg 2005; Hoang et al. 2008;). Semiactive control techniques have been proposed as more efficient approaches for the mitigation of cable vibration and can provide greater damping ratios than passive damping techniques (Johnson 2000; Ni et al. 2002a; Johnson et al. 2003; Chen et al. 2003; Li et al. 2005; Wu and Cai 2007; Weber and Boston 2011; Zhou and Sun 2013). Active control techniques have illustrated superior control performance theoretically among all, although practical implementation of these techniques on real stay cables has been hindered by their complexity, high power demand and potential instability concerns. Nonetheless, the performance from ideal active control techniques has been evaluated as a reference case in studies on semiactive dampers (Johnson et al. 2007; Li et al. 2008; Weber and Boston 2011).

The careful examination of the force–deformation relationship exhibited by active actuators has inspired the solution of negative stiffness dampers to vibration mitigation of stay cables (Li et al. 2008). Shi et al. (2016) were among the first researchers to analyze the dynamic behavior of a stay cable with a passive negative stiffness damper (NSD). They accordingly proposed simple and interesting designs for passive magnetic NSDs (Shi and Zhu 2015, 2017). Shi et al. (2017a) later verified that the optimal damping ratio offered by a passive NSD is four times higher than that offered by a

viscous fluid damper. The results of their numerical comparison indicated that the vibration mitigation performance of a passive NSD installed on a stay cable is comparable with that of active controllers (Shi and Zhu 2017).

Inerter dampers (IDs), which are composed of inerters and viscous dampers connected in parallel, have begun to attract growing interest because their mechanical force–deformation relationship resembles negative stiffness feature. In contrast to NSDs, IDs do not reduce structural stiffness and thus do not compromise the structural stability of stay cables (Shi and Zhu 2018). The effectiveness of IDs in the mitigation of stay-cable vibration has been successfully illustrated numerically (Lazar et al. 2016; Lu et al. 2017) and analytically (Shi and Zhu 2018), but still requires additional experimental verification.

Another exciting advancement in the field of vibration mitigation is the recent development of electromagnetic shunt dampers (EMSDs). EMSDs consist of electromagnetic device connected to external shunt circuits, which control the mechanical behavior of the EMSDs. Some works on the application of EMSDs in the field of civil engineering have been recently reported (Palomera-Arias 2005; Cheng et al. 2009; Cassidy et al. 2011; Shen et al. 2012; Zhu et al. 2012). Given the analogous relationships between mechanical and electrical systems, EMSDs that demonstrate various mechanical behaviors can be obtained by using different electrical elements (Smith 2002). Li and Zhu (2018) employed one type of negative impedance converters (NIC), namely, the NIC with voltage inversion (VNIC), to overcome the performance bottleneck of EMSDs and showed that a single EMSD connected to various shunt circuits could exhibit versatile mechanical behaviors that are analogous to those exhibited by viscous fluid dampers (VFDs), viscoelastic dampers (VEDs), IDs, and tuned inerter dampers (TIDs). The corresponding configurations were designated as

EMSD–VFD, EMSD–VED, EMSD–ID, and EMSD–TID. EMSDs present the following advantages over conventional mechanical dampers:

- EMSDs are lightweight and compact because they are fabricated using electric elements instead of bulky mechanical components.
- EMSDs avoid the problem of overheating, which is commonly encountered by conventional mechanical dampers, by converting mechanical energy to electric energy.
- EMSDs can emulate the behaviors of mechanical elements through the use of electrical components. The mechanical behavior and complexity of the dampers can be flexibly adjusted and modified by simply altering the shunt circuit.

Considering the advantages of EMSD and the great potential of ID in cable vibration mitigation, this paper presents the results of the first experimental study on the control of full-scale bridge cable vibration using the emerging EMSD–ID, which provided high inertance through the use of a capacitor. Damper parameters were optimized on the basis of the numerical models of the cable and damper. Then, the EMSD–ID was designed, fabricated, and tested. The performance of the EMSD–ID was investigated systematically through a series of experiments involving a full-scale model of a stay cable installed with the proposed EMSD–ID. The vibration mitigation performance of the EMSD–ID in various test scenarios was evaluated on the basis of cable responses. The results of the full-scale cable tests validated the superior damping performance of the EMSD–ID. To the best knowledge of the authors, such a full-scale experimental study has not been explored by others so far.

## 2. Cable with ID

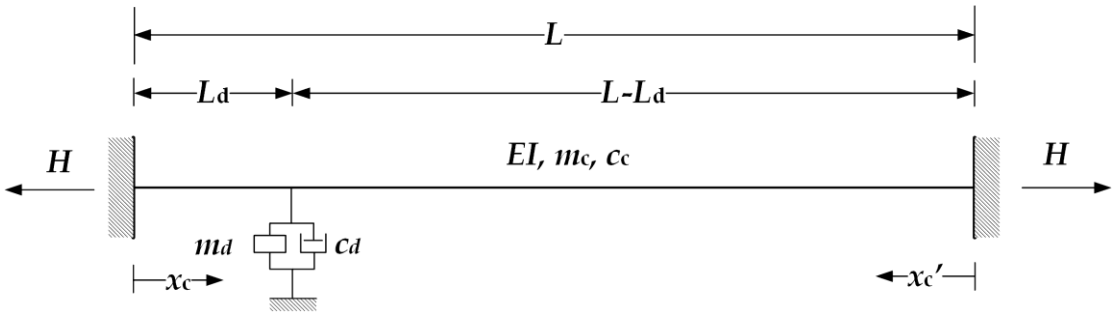


Fig. 1 A taut cable installed with an ID

### 2.1 Numerical Modeling

A taut cable with an ID installed close to one cable end is shown in Fig. 1. In this figure, $H$ is the cable tension force, $m_c$ is the mass per unit length, $c_c$ is the damping per unit length, $EI$ is the flexural rigidity, $L$ is the total cable length, and $L_d$ is the distance from the ID to the nearest anchorage, $x_c$ is the coordinate measured from the near anchorage side. A numerical cable model generated using the unified finite difference method (Mehrabi and Tabatabai 1998) was adopted in this work. The efficacy and accuracy of this model has been previously validated through the dynamic simulation of a stay cable from the Stonecutters Bridge of Hong Kong (Shen and Zhu 2015). A brief description of the unified finite difference method is provided in this section. Additional detailed information was provided by Shi et al. (2017a; b).

The transverse vibration of a taut cable with an ID installed at $L_d$ position can be described by Eqs. (1) and (2),

$$H\frac{\partial^2 u(x_c,t)}{\partial x_c^{\,2}}-\frac{\partial^2}{\partial x_c^{\,2}}\left(EI\frac{\partial^2 u(x_c,t)}{\partial x_c^{\,2}}\right)-c_c\frac{\partial u(x_c,t)}{\partial t}-m_c\frac{\partial^2 u(x_c,t)}{\partial t^2}=F(t)\delta(x_c-L_d) \quad (1)$$

$$F(t)=m_d\ddot{u}(L_d,t)+c_d\dot{u}(L_d,t) \quad (2)$$

where $u(x_c,t)$ is the transverse displacement at location $x_c$ and instant $t$; $\delta(\cdot)$ is the Dirac delta function; $F(t)$ is the damper force at instant $t$; and $m_d$ and $c_d$ are the inertance and damping coefficients of the ID, respectively.

The finite difference method can be used to discretize the cable into multiple elements $n$ with element length $a$. Consequently, the stiffness matrix of an uncontrolled stay cable with a uniform cross-section can be expressed as:

$$\mathbf{K}=\begin{bmatrix} Q & D & W & & & 0 \\ D & S & D & W & & \\ W & D & S & D & \ddots & \\ & W & \ddots & \ddots & \ddots & W \\ & & \ddots & \ddots & S & D \\ 0 & & & W & D & Q \end{bmatrix} \tag{3}$$

where

$$S=\frac{6EI}{a^3}+\frac{2H}{a},\ D=-\frac{4EI}{a^3}-\frac{H}{a},\ W=\frac{EI}{a^3} \tag{4}$$

and $Q$ is dependent on the boundary conditions of the cable.

$$\begin{aligned} &\text{For a fixed connection,} && Q=\frac{7EI}{a^3}+\frac{2H}{a}. \\ &\text{For a pinned connection,} && Q=\frac{5EI}{a^3}+\frac{2H}{a}. \end{aligned} \tag{5}$$

In Eq. (3), the contribution of the flexural rigidity of a cable, which has a considerable effect on the dynamics and damping performance of a stay cable (Ni et al. 2002b), is considered.

The mass matrix is established as the lumped mass model

$$\mathbf{M}=\mathbf{I_N}\cdot ma \tag{6}$$

where $\mathbf{I_N}$ is a $n\times n$ identity matrix. Given the stiffness and mass matrices, the damping matrix $\mathbf{C}$ can be constructed in accordance with Rayleigh damping.

The installation of the ID on the cable is reflected by the addition of extra inertance and damping coefficients at the damper location in the model. If the damper is installed at the $j^{th}$ node, the mass and damping matrices should be updated as

$$m'_{jj} = m_{jj} + m_d \tag{7}$$

$$c'_{jj} = c_{jj} + c_d \tag{8}$$

where $m_{jj}$ and $c_{jj}$ are the $j^{th}$ diagonal elements in matrices $\mathbf{M}$ and $\mathbf{C}$ of the uncontrolled cable, respectively, and $m'_{jj}$ and $c'_{jj}$ are the updated diagonal elements in mass matrix $\mathbf{M'}$ and damping matrix $\mathbf{C'}$ of the cable installed with an ID. All other elements in $\mathbf{M'}$ and $\mathbf{C'}$ were kept constant. Given the mass, damping, and stiffness matrices, the dynamic simulations of the cable installed with an ID can be performed.

Notably, inertance is essentially different from mass. The former corresponds to the relative acceleration between two nodes, whereas the latter corresponds to the absolute acceleration of a single node. The ID should be installed between the cable and bridge deck. The absolute acceleration of the cable at the damper location then becomes the relative acceleration between the two ends of the damper. Consequently, in this special case, the effect of inertance is similar to that of the addition of mass.

### 2.2 Parameter Optimization

An ID can provide the optimal damping performance only to a single target vibration mode of the stay cable (Shi and Zhu 2018). Optimization is achieved when two adjacent wave numbers (or complex frequencies) become identical (i.e., same frequency and damping ratio), wherein the two wave numbers correspond to a single mode of the original cable. Consequently, the damping ratio of the target mode can be maximized when the inertance and damping coefficients ($m_d$ and $c_d$) are optimally

tuned. Vibration mitigation performance will deteriorate if the parameters exceed their optimal values.

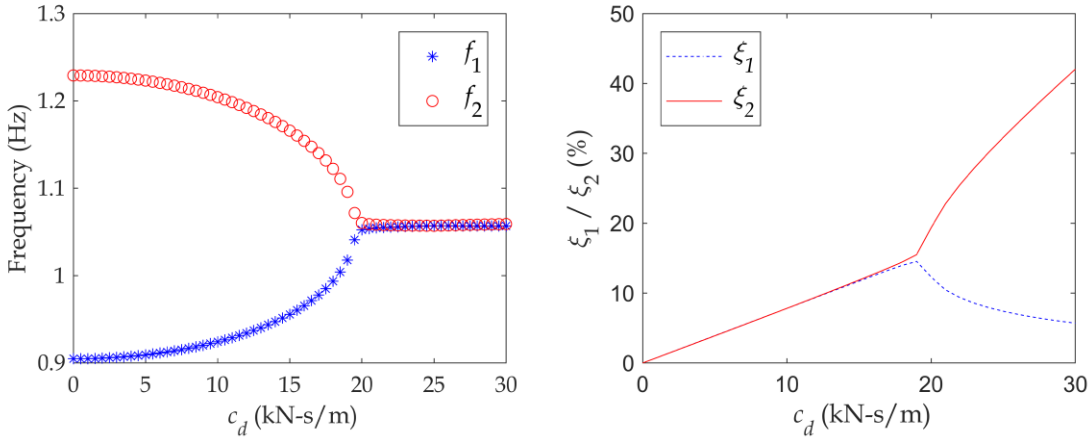


(a) (b)

Fig. 2 (Color) Variation of (a) frequencies; and (b) damping ratios with the damping coefficients of ID ($m_d$= 4.3 t)

Shi and Zhu (2018) introduced a numerical method for the parameter optimization of the ID of a cable. Their numerical method is based on the variation in the loci of the wave numbers. In this study, the first vibration mode was selected as the target mode. By considering the parameters of the full-scale stay cable described in Section 4.1, the optimal inertance and damping coefficients were determined as $m_d$ = 4.3 t and $c_d$ = 18.8 kN−s/m, respectively, when the ID was installed at the 5% location. Fig. 2 shows the variation in the first two frequencies and damping ratios with the increment in damping coefficients when the inertance coefficient is fixed at the optimal value of $m_d$ = 4.3 t. Notably, the actual damping ratio of the target mode is controlled by the lower one of $\zeta_1$ and $\zeta_2$. The optimal damping ratio can be obtained when the two frequencies meet each other. The achievable maximum damping ratio of the fundamental mode versus various inertance coefficients is shown in Fig. 3. A pure viscous damper ($m_d$ = 0 t) attains the maximum damping ratio of $\zeta_1$=2.6% when it is located at the 5% location. The maximum damping ratio of the cable provided by an ID with $m_d$ = 4.3 t can reach

11%, which is 4.23 times that of a traditional viscous damper. Inertance coefficients with values that differ from the optimal value offer lower damping ratio but remain more effective than the pure viscous case. This observation illustrates the benefits of using ID in cable vibration mitigation.

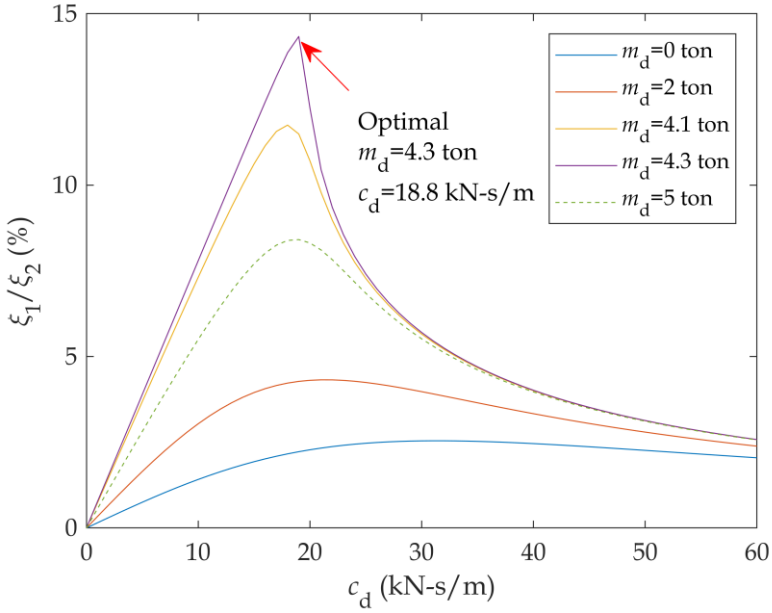


Fig. 3 (Color) Variation of the maximum achievable damping ratio with the inertance coefficient of ID (the damper location at 5% of cable length)

## 3. Electromagnetic Shunt Damper–Inerter Damper

The EMSD–ID is an innovative and efficient way for emulating the mechanical behavior of an ID with EMSD (Li and Zhu 2018). The concept, design, fabrication and characterization of the EMSD–ID used in the full-scale experiment are presented in this section.

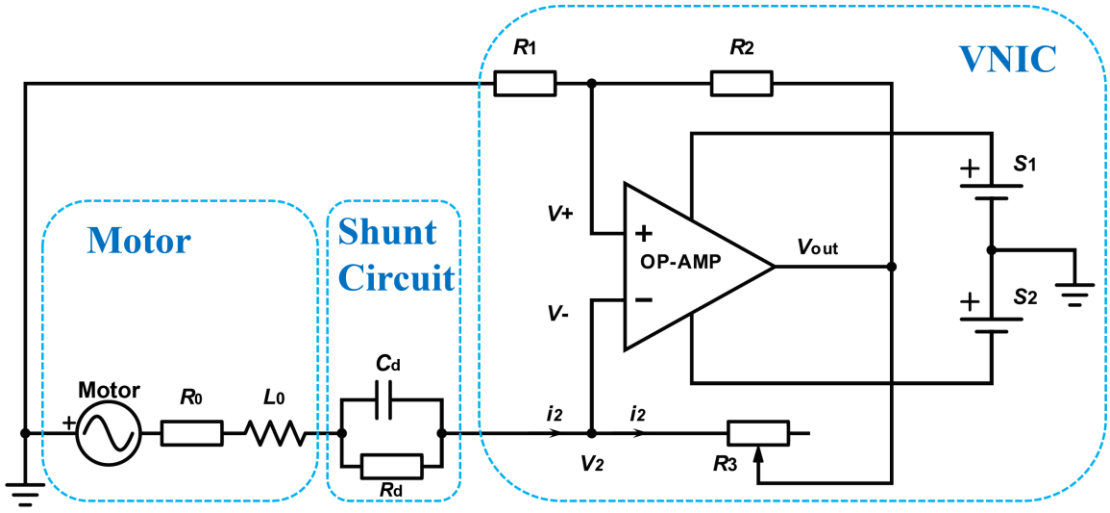


Fig. 4 (Color) EMSD-ID with VNIC. $R_d$ in the shunt circuit is optional. It is added only when a larger dampign ratio is desired.

### 3.1 Concept

An EMSD comprises two connected parts, namely, an electromagnetic device and external shunt circuit. The former is an electromechanical coupling device, and the latter involves common electric components, such as resistors, inductors, and capacitors. The simple analogous relationship between the mechanical system and its electrical equivalents was first presented in the 1940s (Bloch 1945) and has been recently discussed by different researchers (e.g., Li and Zhu 2018)

$$\begin{aligned} m &= K_{\text{em}}^2 \cdot C \\ c &= K_{\text{em}}^2 / R \\ k &= K_{\text{em}}^2 / L \end{aligned} \tag{9}$$

where $m$, $c$, and $k$ represent the inertance, damping, and stiffness coefficients, respectively; and $C$, $R$, and $L$ represent the capacitance, resistance, and inductance values, respectively; and $K_{\text{em}}$ is the motor constant of an electromagnetic device. According to Eq. (9), the inertance and damping components of a mechanical ID can be emulated by their electrical equivalents in the EMSD–ID.

However, this emulation is valid only when electric impedance consists of a single term in Eq. (9). In practice, electrical elements, such as electromagnetic devices and inductors, are associated with inner resistances (i.e. $R_0$ in Fig. 4). The serial connection of $R_0$ with the shunt circuit is equivalent to the connection of an undesired damper between the ID and host structure. Consequently, the presence of $R_0$ will always degrade damper performance and prevent the EMSD from exhibiting the desired performance. Thus, a VNIC was introduced by Li and Zhu (2018) into the shunt circuit as a simple and practical solution to these limitations. The schematic of the EMSD–ID with VNIC is shown in Fig. 4. VNIC functions as the negative resistance $R_{\mathrm{VNIC}}$

$$R_{\mathrm{VNIC}} = -\frac{R_1 R_3}{R_2} \tag{10}$$

where the negative resistance $R_{\mathrm{VNIC}}$ is determined by three resistors $R_1$, $R_2$, and $R_3$. Consequently, damper performance can be enhanced by partially compensating for the adverse effect of $R_0$ resulting in a new total equivalent resistance $R_{\mathrm{t}} = R_0 - \left|R_{\mathrm{VNIC}}\right|$. When $R_{\mathrm{t}}$ becomes adequately small, satisfactory emulation of ID using EMSD-ID can be guaranteed to manipulate the inertance and damping coefficient values by adjusting capacitance $C_{\mathrm{d}}$ and resistance $R_{\mathrm{d}}$ of the shunt circuit in reference to Eq. (9). In particular for EMSD−ID, the adoption of $R_{\mathrm{d}}$ is optional, and $R_{\mathrm{d}}$ will only be connected when increased damping is desired. Li and Zhu (2018) provided a detailed discussion of EMSD with VNIC. It is noteworthy that under low frequency excitations, the small coil inductance of an electromagnetic device is often ignorable. Thus, the EMSD-ID presented in this study is not a resonant damper.

### 3.2 Design of the EMSD–ID Prototype

The electromagnetic device can be a simple electromagnetic non-commutated DC linear motor that enables conversion between the kinetic energy of a host structure and electrical energy in the shunt circuit. The electromechanical coupling relationship is given by the motor constant $K_{em}$, a crucial parameter determining the conversion ability of the motor. The motor constant is an inherent parameter of the electromagnetic device and is independent of the external circuit design (Zhu et al. 2012). Its mathematical relations are provided in Eqs. (11) and (12), as follows:

$$U = K_{em}\dot{x} \tag{11}$$

$$F = K_{em}I \tag{12}$$

where $U$ is the back electromotive force (EMF), $F$ is the electromagnetic force generated by the motor with current $I$ flowing through the motor coil, and $\dot{x}$ is the relative velocity between two motor nodes.

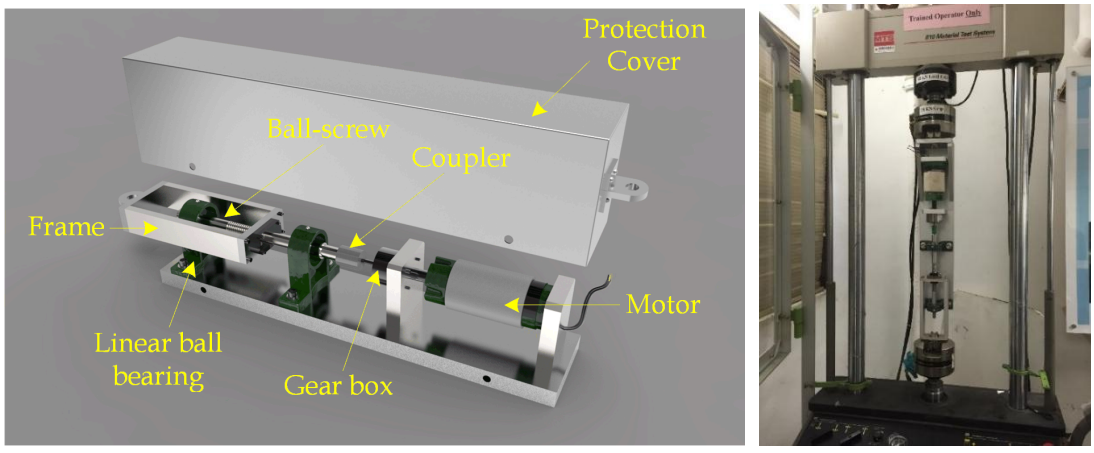


(a) (b)

Fig. 5 (Color) EMSD–ID prototype designed for a full-scale cable: (a) 3D concept illustration; and (b) the tested prototype.

As revealed in Eqs. (11) and (12), a sufficiently large motor constant $K_{em}$ is necessary if a large control force is desired in full-scale applications. An ordinary electromagnetic non-commutated DC linear motor typically cannot provide a large $K_{em}$ value. In this study, a new configuration of the electromagnetic device was designed to increase the motor constant. The design is shown in Fig. 5. It consists of two key modules, namely, a ball-screw module that transforms linear motion into rotatory motion, and a rotary DC motor connected to a gear box. The prototype had a gear ratio of $\alpha = 12:1$. The ball-screw and gear box modules can effectively accelerate the rotatory speed of the DC motor to amplify the motor constant $K_{em}$ considerably. The three-dimensional schematic of the conceptual design is shown in Fig. 5(a).

The EMSD–ID prototype can simply be obtained by connecting the electromagnetic device described above to a capacitor and VNIC. The prototype was fabricated and tested in the laboratory before it was applied in the full-scale experiment. The experimental results are detailed in the following subsection.

### 3.3 Experimental Characterization of the EMSD–ID

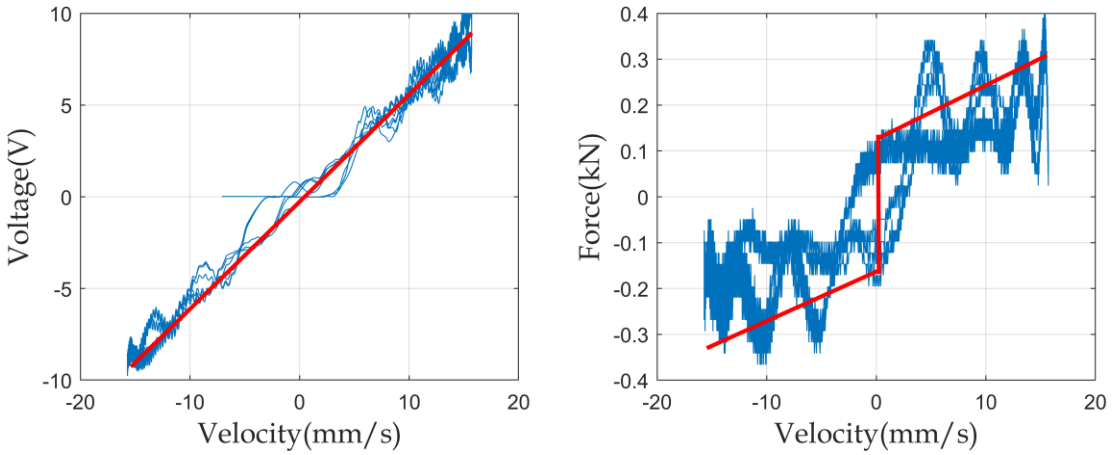


(a) (b)

Fig. 6 (Color) Experimental results of the EMSD without external circuit (f = 0.5 Hz, d = 5 mm): (a) open-circuit voltage versus velocity relationship; and (b) damper force versus velocity relationship.

### 3.3.1 EMSD without an External Circuit

The fabricated electromagnetic device was first cyclically tested on an MTS machine (MTS Systems, Eden Prairie, Minnesota) [as shown in Fig. 5 (b)] while unconnected to any external circuit (i.e., open circuit). The results obtained with loading frequency of $f$ = 0.5 Hz and loading amplitude of $d$ = 5 mm are provided in Fig. 6. The relation between the open circuit voltage (i.e., electromotive force) and damper velocity is shown in Fig. 6(a). In accordance with Eq. (12), the slope of the regression line in Fig. 6(a) provided the motor constant $K_{em}$ = 640 V−s/m (or N/A). This result proves that the adopted design could effectively increase the motor constant to a sufficiently high level.

The force–velocity relationship of the electromagnetic device is shown in Fig. 6(b). The parasitic damping force observed in Fig. 6(b) mainly originated from mechanical friction and motor iron loss in the absence of connections to any circuit. Jagged force was generated by the ball-screw and gear box setup, while its magnitude is often smaller than the damper force described in the following sections. Parasitic damping can be modelled as the superposition of viscous damping and Coulomb damping (Zhu et al., 2012). Under harmonic oscillation, the equivalent viscous damping coefficient for parasitic damping $c_p$ can be computed by using the following formula (Zhu et al., 2012)

$$c_p = \frac{2k_1}{\pi^2 fd} + k_2 \tag{13}$$

where $f$ and $d$ is the frequency and magnitude, respectively, of harmonic oscillation; $k_1$ is the magnitude of frictional force; and $k_2$ represents the viscous damping coefficient. Two damping constants could be identified from Fig. 6(b) as $k_1$ = 0.16 kN and $k_2$ = 9 kN−s/m through regression analysis (red line), where the friction magnitude $k_1$ and the viscous damping coefficient $k_2$ correspond to the y-intercept and slope, respectively.

The equivalent parasitic damping coefficient was calculated as $c_p = 22$ kN−s/m by using Eq. (13).

The parameters of the electromagnetic motor are summarized in Table 1. Inner motor resistance and inductance were measured by using an LCR meter (Model No. Hoiki 3522-50, HIOKI E.E., Nagano, Japan). Low inner inductance can be ignored in low-frequency vibration.

Table 1 EMSD configuration parameters

| Parameter | Values |
|---|---|
| Motor constant ($K_{em}$) | 640 V-s/m (or N/A) |
| Parasitic friction ($k_1$) | 0.16 kN |
| Parasitic damping coefficient ($k_2$) | 9 kN-s/m |
| Equivalent damping coefficient ($c_p$) | 22 kN-s/m |
| Motor inner resistance ($R_0$) | 7.5 Ω |
| Motor inner inductance ($L_0$) | 13.35 mH |

### 3.3.2 Test of EMSD–ID

The EMSD was connected to the VNIC and capacitors to form the EMSD–ID and then tested again on the MTS machine. The results of this experiment are presented in this subsection.

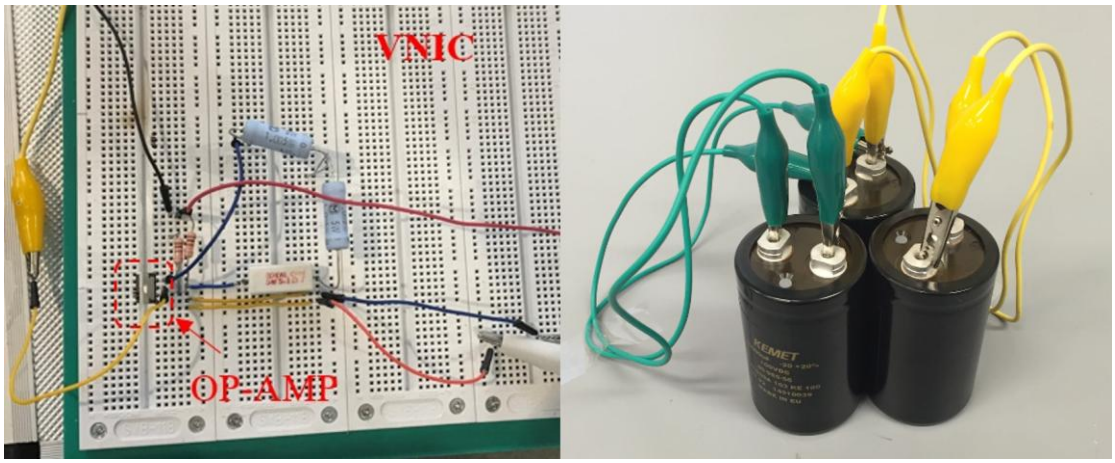

(a) (b)

Fig. 7 (Color) External shunt circuit used in EMSD–ID: (a) VNIC on the breadboard; and (b) capacitors [KEMET 0.01 F (Fort Lauderdale, Florida) each].

The VNIC assembly on a breadboard is shown in Fig. 7(a). The voltage distribution resistors $R_1$ and $R_2$ were selected with values of 1 MΩ each. A high power operational amplifier (APEX PA75CD, Tucson, Arizona) with maximum current limit of 2.5 A was used. As shown in Table 1, the motor coil resistance was $R_0$ = 7.5 Ω. The VNIC was intended to counteract motor inner resistance to an adequately small value of 0.2 Ω and enhance control performance.

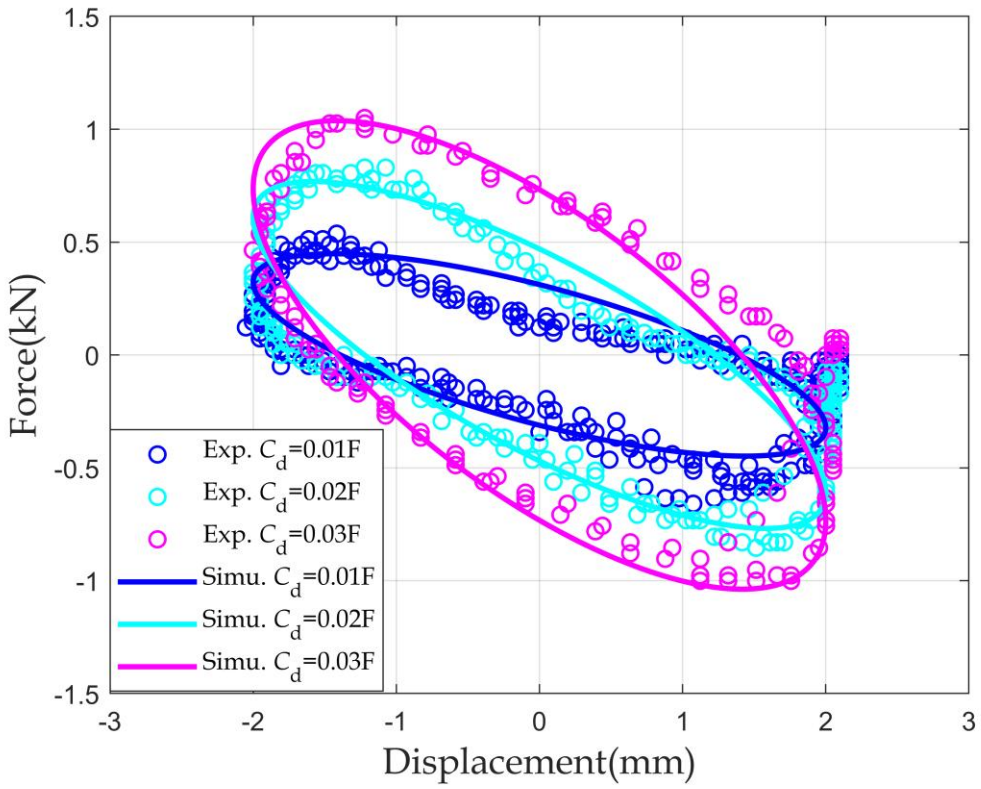


Fig. 8 (Color) Damper force–displacement relationship of EMSD–ID with different capacitance values.

The capacitors used in the shunt circuit are shown in Fig. 7(b). Each capacitor had the capacitance of $C_d$ = 0.01 F. Thus, the EMSD–ID was tested with capacitances of $C_d$ = 0.01, 0.02, and 0.03 F. In accordance with Eq. (9), these capacitance values emulated

the three inertance values of $m_d$ = 4.1, 8.2 and 12.3 t. The force–displacement hysteresis loops obtained through the cyclic tests are shown in Fig. 8. The theoretical and experimental results showed good agreement given that the theoretical results were obtained on the basis of the above theoretical inertance values.

Notably, large inertance (12.3 t) was emulated simply through the use of the three capacitors. The total volume and weight of three capacitors were 0.001 $m^3$ and 660 g separately. The ratio of the achieved inertance to the capacitor mass reached 18,636. This result validates the advantage of the EMSD–ID in large-scale applications. Furthermore, the emulated inertance can be conveniently adjusted by simply changing the capacitance in the external shunt circuit connected to the same prototype. A wide range of inertance can be emulated by using commercially available capacitors. Given that the electromagnetic device does not require modification, it can enable the production of standardized EMSDs for different applications. From this perspective, the EMSD–ID exhibits considerably higher efficiency and flexibility than conventional IDs.

In the case of a single capacitor ($C_d$ = 0.01 F), the theoretically predicted inertance was $m_d$ = 4.1 t, which approaches the optimal inertance value of $m_d$ = 4.3 t described in Section 2.2. Thus, this EMSD–ID case was adopted in the full-scale experiment. The consistency between the experimental and numerical results shown in Fig. 8 confirms the successful realization of an inertance of $m_d$ = 4.1 t and equivalent parasitic damping of $c_d$ = 22 kN−s/m. Nevertheless, both values deviated from the optimal values of $m_d$ = 4.3 t and $c_d$ = 18.8 kN−s/m. This deviation resulted in suboptimal control performance in the full-scale cable experiment.

## 4. Setup of the Full-scale Cable Experiment

OVM Co. Ltd. (Hubei, Central China), a major cable manufacturer and supplier in China, was approached for collaboration. The full-scale experiment was conducted on a stay cable with a length of 135 m and installed with the designed EMSD–ID. The experiment was conducted in the factory of OVM Co. Ltd. to facilitate installation, instrumentation, and dynamic testing.

### 4.1 Cable Parameters

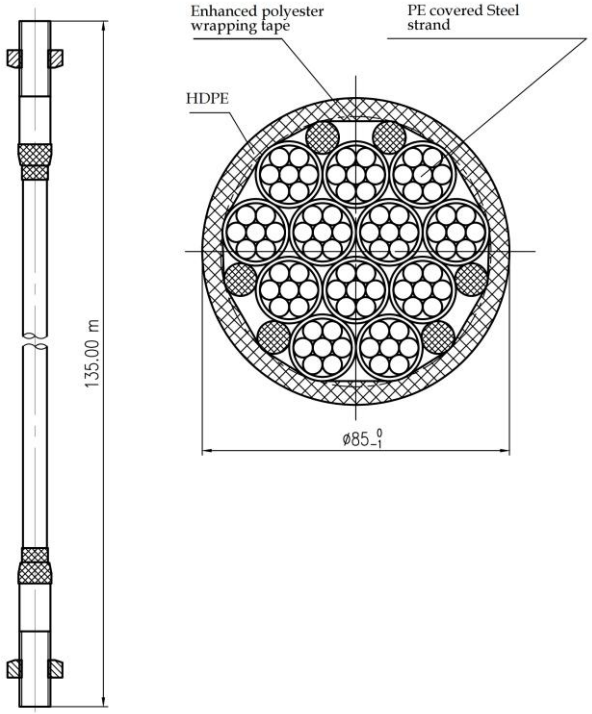


Fig. 9 Cable cross section. (Reprinted with permission from OVM Co. Ltd. 2014.)

The cross-section of the OVM GJ 15-12 (OVM Co. Ltd., 2014) cable, which represents a typical stay cable used in real cable-stayed bridges, is shown in Fig. 9. The section consisted of 12 cable strands compactly twisted together to form the cable body which was coated with a high-density polyethylene (HDPE) protection layer. Table 2 presents the major parameters of a single strand and the whole cable.

Table 2 Cable Parameters

| Item | s | Value | Unit |
|---|---|---|---|
| Single strand | Strand diameter ($D_n$) | 15.2 | mm |
| | Allowed bias of diameter | -0.2~+0.4 | mm |
| | Cross sectional area | 140 | $mm^2$ |
| | Cable strand unit mass ($m_s$) | 1101 | g/m |
| | Stress capacity | 1860 | MPa |
| | Overall strand maximum force | 260~274 | kN |
| | Elastic Modulus ($Es$) | 195±10 $e^{11}$ | Pa |
| Cable | Cable unit mass ($m$) | 16.65 | kg/m |
| | Cable diameter ($D$) | 85 | mm |
| | Cable tension force ($T$) | 1200 | kN |
| | Yielding load | 3120 | kN |
| | Cable length ($L$) | 135 | m |
| | Young's modulus ($E$) | 195 | GPa |

The schematic and photograph of the 135 m-long stay cable in the laboratory are shown in Figs. 10 and 11(a), respectively. Given that the end rotation of the cable was prevented by using the steel end plates shown in Fig. 11(b), both cable ends were treated as fixed boundary conditions. A tension of 1,200 kN was applied to the stay cable by using a cable tensioner. The first three natural frequencies of the tested cable were estimated as 1.083, 2.208, and 3.341 Hz on the basis of the numerical models (Section 2.1) with the EMSD–ID ($m_d$ = 4.1 t) installed at the 5% location and in consideration of the flexural rigidity of the cable.

## 4.2 Instrumentation

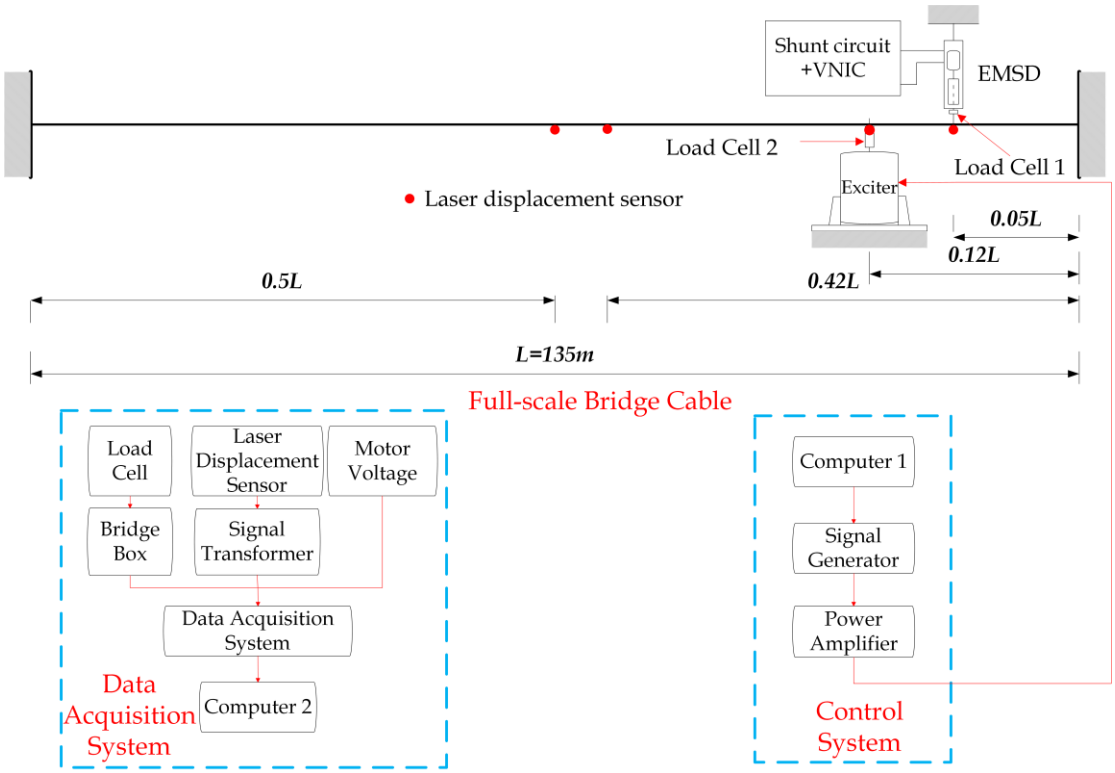


Fig. 10 (Color) Experimental setup in the cable tests.

The layout of the experimental setup is shown in Fig. 10, and additional photographs of the experimental conditions are shown in Fig. 11. The damper and exciter were installed at the 0.05$L$ and 0.12$L$ positions from the right anchorage, respectively. Four laser displacement sensors were used to record the displacement responses of the cable at the damper, exciter, midspan, and 0.42$L$ locations. The input signal generated by the signal generator was amplified and fed into the exciter to apply the target excitation to the cable. The voltage and current from the electromagnetic motor and in the shunt circuit were also measured for circuit analysis. The collected data were received and stored by a data acquisition system.

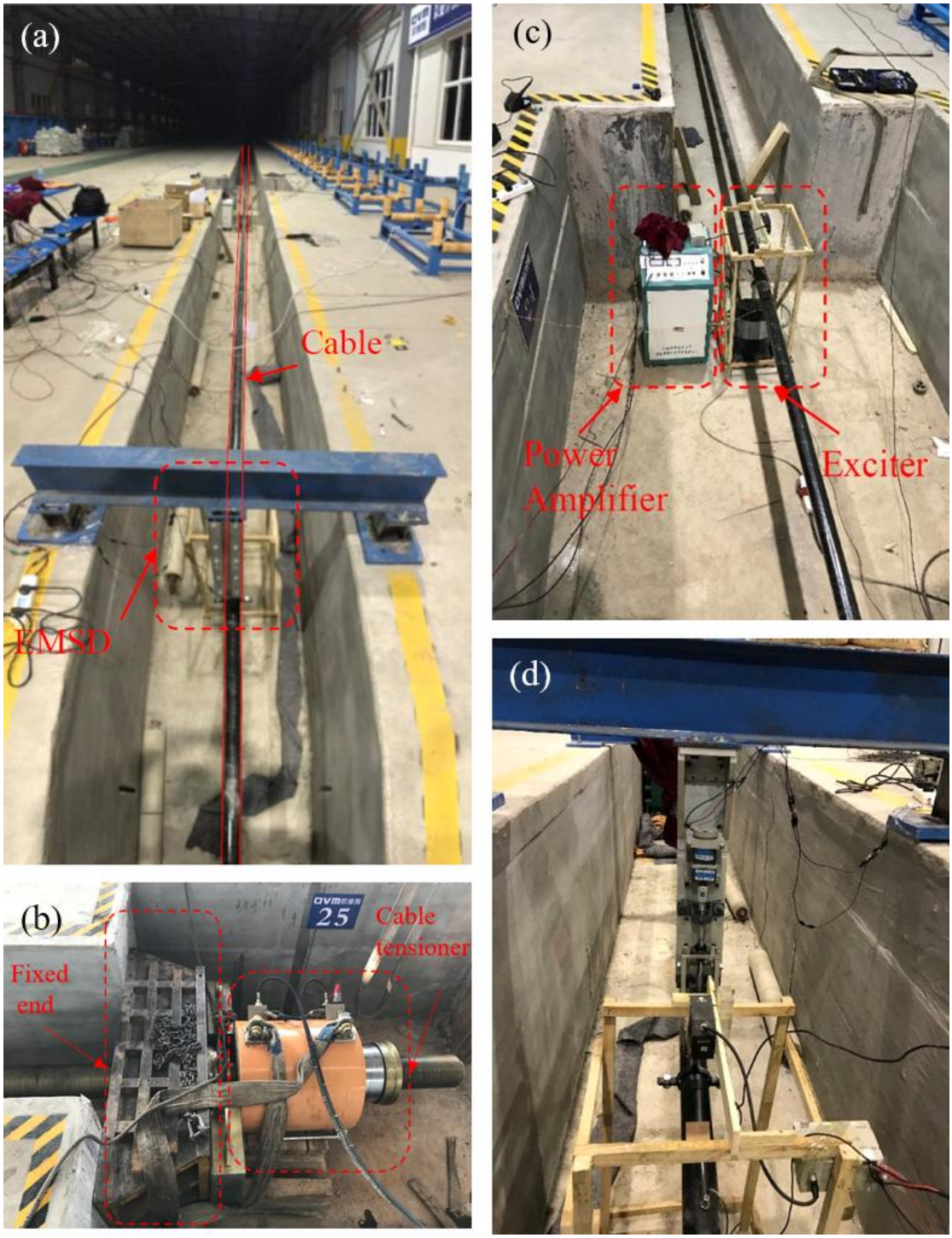


Fig. 11 (Color) Full-scale bridge cable experimental setup: (a) a 135-m-long bridge cable being tested; (b) end fixture and cable tensioner; (c) dynamic exciter with power amplifier; and (d) front view of EMSD–ID on the cable.

### 4.3 Test Scenarios

The test scenarios in the full-scale stay cable experiment, including the cases without a control, with open-circuit EMSD contributing only parasitic damping, and

with the EMSD–IDs involving different combinations of $C_d$ and $R_d$ values, are listed in Table 3. The corresponding equivalent mechanical coefficients $c_d$ and $m_d$ were calculated in accordance with Eq. (9). The equivalent parasitic damping coefficient $c_p$ of 22 kN−s/m was the lower limit of mechanical damping. As shown in Fig. 4, a larger mechanical damping coefficient could be obtained by connecting a resistor in parallel with the capacitor.

Table 3 Testing scenarios of the cable with EMSD-ID and the corresponding damping ratios

| Case | Circuit Conditions ($C_d + R_d$) | Equivalent Mechanical Coefficients | Damping Ratio (%) | |
|---|---|---|---|---|
| | | | Experimental [a] | Numerical [b] |
| 1 | Without damper | — | 0.2 | 0.2 |
| 2 | Open circuit with parasitic damping only | $c_d$ = 22 kN-s/m | 2.3 | 2.0 |
| 3 | 0.01 F | $m_d$ = 4.1 t, $c_d$=22kN-s/m | 8 | 8.98 |
| 4 | 0.01 F+97 Ω | $m_d$ = 4.1 t, $c_d$=26.4 kN-s/m | 7.2 | 6.73 |
| 5 | 0.01 F+47 Ω | $m_d$ = 4.1 t, $c_d$=30.7 kN-s/m | 6.3 | 5.49 |
| 6 | 0.01 F+23.5 Ω | $m_d$ = 4.1 t, $c_d$=39.4 kN-s/m | 4.8 | 4.07 |

a. The experimental damping ratios were identified from the free-vibration responses from the damper position.

b. The numerical damping ratio were identified from the numerical model introduced in Section 2.1 and was shown in Fig. 14.

The stay cable was tested under free vibration, sinusoidal sweeping excitation, and random excitation. However, the random vibration responses in all the cases with control were too small for evaluation, given the limited output power of the exciter.

## 5. Experimental Results

The results from the full-scale cable tests were compared with the numerical results. The discussion of the results is presented in this section.

### 5.1 Free Vibration

Free vibrations were generated by first artificially exciting the cable to high vibration amplitudes and then suddenly releasing excitation. Only the first-mode vibration could be generated through artificial excitation.

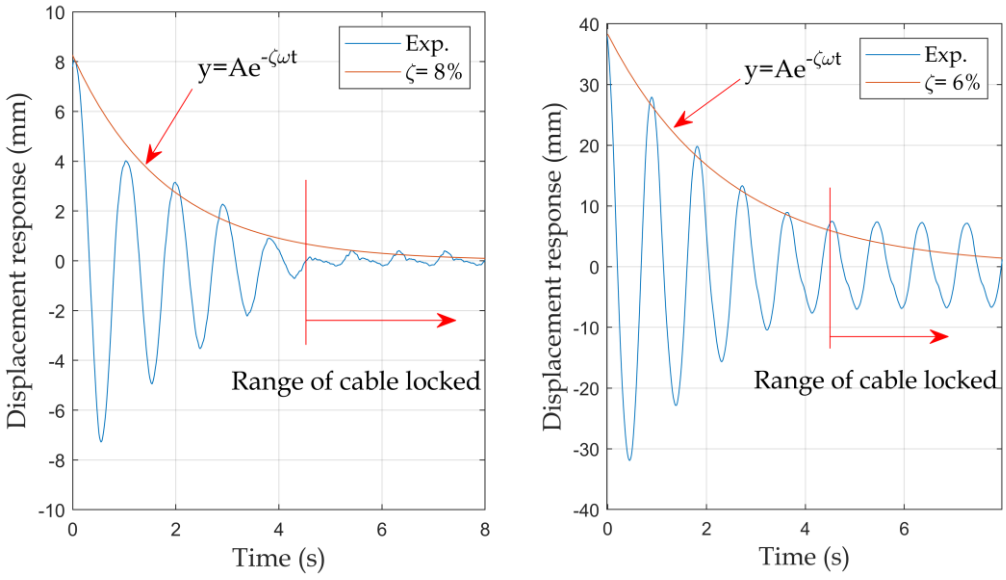


(a) (b)

Fig. 12 (Color) Free-vibration responses in Case 3 (Cd = 0.01 F): (a) at the damper position; and (b) at the 0.42L position.

Free vibration quickly returned to the static state because of the damping effect. The damping ratio $\zeta$ can be computed on the basis of the free vibration attenuation rate:

$$\zeta = \frac{1}{2\pi n} \ln\left(\frac{x_i}{x_{i+n}}\right) \tag{14}$$

where $x_i$ and $x_{i+n}$ represent the amplitudes of the $i^{\text{th}}$ and $(i+n)^{\text{th}}$ peaks. This estimation is acceptable if the damping ratio is less than 0.1 (Meirovitch 2001). Accordingly, the damping ratio in Case 3 ($C_d$ = 0.01 F) was estimated as 8% and 6% on the basis of the free vibration responses shown in Fig. 12(a) and (b), respectively. The vibration attenuation rate shown in Fig. 12(a) slightly differed from that shown in Fig. 12(b); in general, vibration attenuated more rapidly at the damper position than at other positions. The logarithm attenuation curves corresponding to these two attenuation ratios are also shown in the figure and correspond well to the results obtained from Eq. (14).

Discrepancy, however, can be observed in the tail range shown in Fig. 12. From 4.5 s, damper displacement became minimal, and the damper was nearly locked because of the static friction effect (Fig. 12(a)). Consequently, the damper could no longer dissipate any energy, and the cable returned to a low damping state. The cable vibrations at the remaining positions attenuated slowly as the damper position locked (Fig. 12(b)).

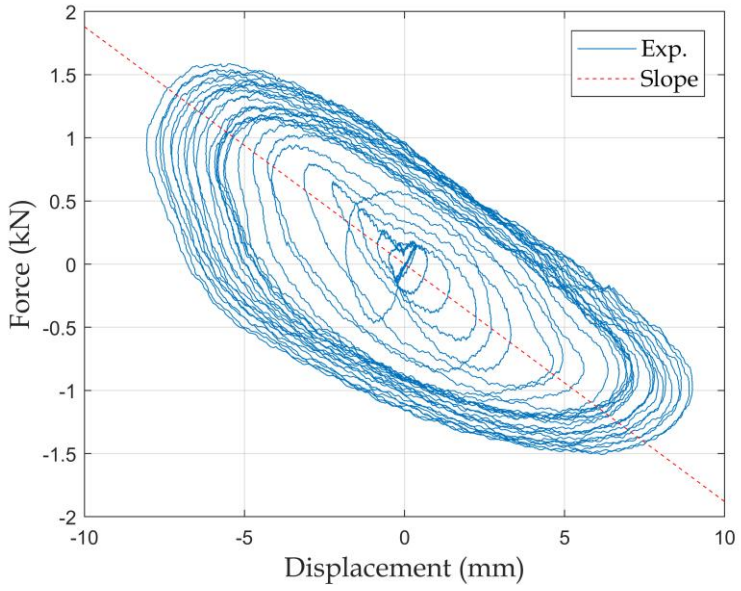

Fig. 13 (Color) Damper force–displacement relationship measured during free vibration in Case 3.

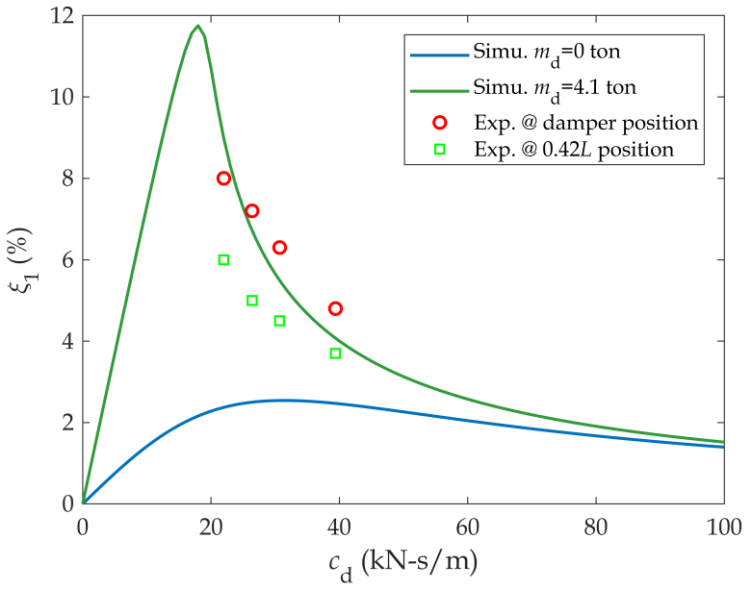


Fig. 14 (Color) Comparison of the experimental and theoretical damping ratios of the cable with EMSD–ID (md = 4.1 t).

The in situ damper force–displacement relationship measured under the free vibration test in Case 3 ($C_d$ = 0.01 F) is shown in Fig. 13. The equivalent inertance and damping coefficients could be estimated as $m_d$ = 4.1 t and 22 kN−s/m, respectively, on the basis of slope of the red dashed line and the area of the ellipse. These values match those obtained in the damper tests on the MTS machine described in Section 3.3.

Similarly, the damping ratio of the cable could be identified in Cases 4–6. In these cases, the damping coefficients varied through the addition of the corresponding parallel resistor value. All cases with free vibration were tested thrice to ensure the accuracy of the results. The average damping ratios obtained in these tests are summarized in Table 3.

The variation in the experimental damping ratio of the cable with the variation in the damping coefficient of the damper is shown in Fig. 14. The theoretical curve

corresponding to inertance $m_d$ = 4.1 t is shown for comparison. A fair agreement between the experimental and theoretical results was observed. In addition, the curve with $m_d$=0 t, which corresponds to the case with a traditional viscous fluid damper, is provided as a reference in Fig. 14. The maximum achievable damping ratio read as 2.54% at the optimal damping coefficient $c_d$=31 kN-s/m. Even though the EMSD–ID in the experiment represented only a suboptimal case, the experimentally obtained damping ratio for the EMSD-ID was still up to 8%, over three times the optimal value achievable by a traditional viscous damper.

### 5.2 Sweep Excitation

Sinusoidal sweeping excitations were applied to the cable at the incremental rates of 0.005 Hz/s for Case 2 (with parasitic damping only) and 0.01 Hz/s for Case 3 (with the EMSD–ID; $C_d$ = 0.01 F). The input signal gain was kept constant in all cases to enable comparison. Given the low damping of the uncontrolled cable in the absence of the EMSD–ID, however, the cable vibration exceeded the limited stroke of the exciter, and no satisfactory measurements were obtained for Case 1 (without control).

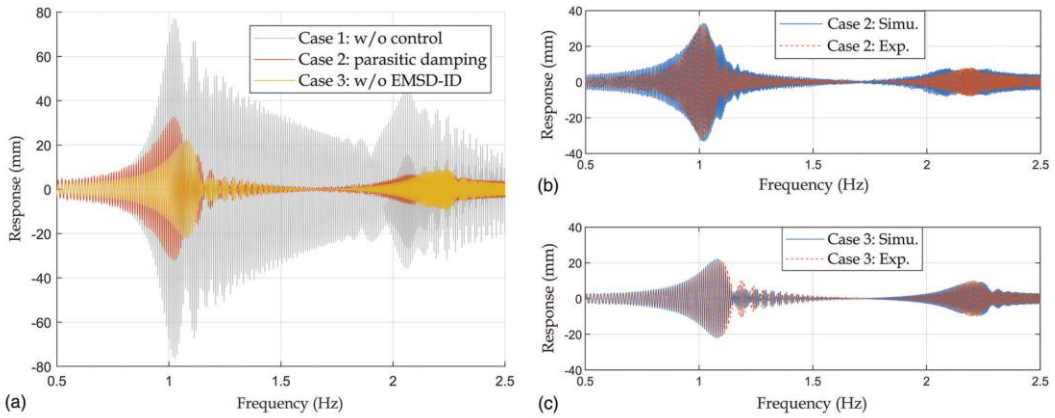


Fig. 15 (Color) Comparison of cable displacement responses at the 0.42L position in different cases: Case 1, without control; Case 2, with parasitic damping only; and Case 3, with EMSD–ID: (a) numerical simulation (at the 0.42L position); (b) experimental

and numerical results, Case 2 (at the 0.42L position); and (c) experimental and numerical results, Case 3 (at the 0.42L position).

A comparison of the cable displacement responses at the 0.42*L* position in the three cases (Case 1–3) is provided in Fig. 15. Results from the numerical simulations, which adopted the excitation forces measured in the experiments as the input, are presented in Fig. 15(a). The comparison between experimental and simulation results is shown in Fig. 15(b) and (c), where the experimental results for Case 1 were not included due to aforementioned reasons. From Fig. 15(a), the peak displacement that corresponded to the first mode resonance reached 76 mm in Case 1. The peak displacements in Case 2 and Case 3 decreased to 35.8 and 21.6 mm, respectively, and corresponded to reductions of 53% and 72% in amplitude, respectively. These results clearly illustrate the superior performance of the EMSD–ID in controlling the vibration of the stay cable. The agreement between numerical and experimental results shown in Fig. 15(b) and (c) further emphasized the functionality and soundness of the proposed EMSD–ID setup and the adopted numerical model.

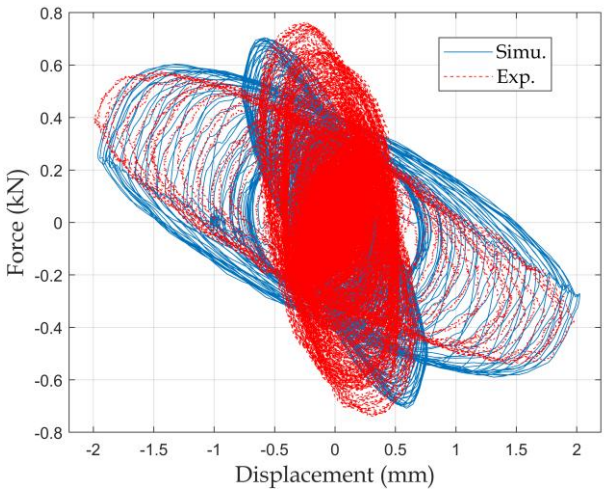


Fig. 16 (Color) Force–displacement relationships of EMSD–ID in Case 3.

The damper force–displacement relationship between the numerical and experimental results at the damper position in Case 3 were also compared and shown

in Fig. 16. Both damping and inertia characteristics were apparent accordingly to the hysteresis loop; the frequency-dependent behavior of ID illustrated by the appearance of distinct slopes corresponds to first- and second-mode resonance.

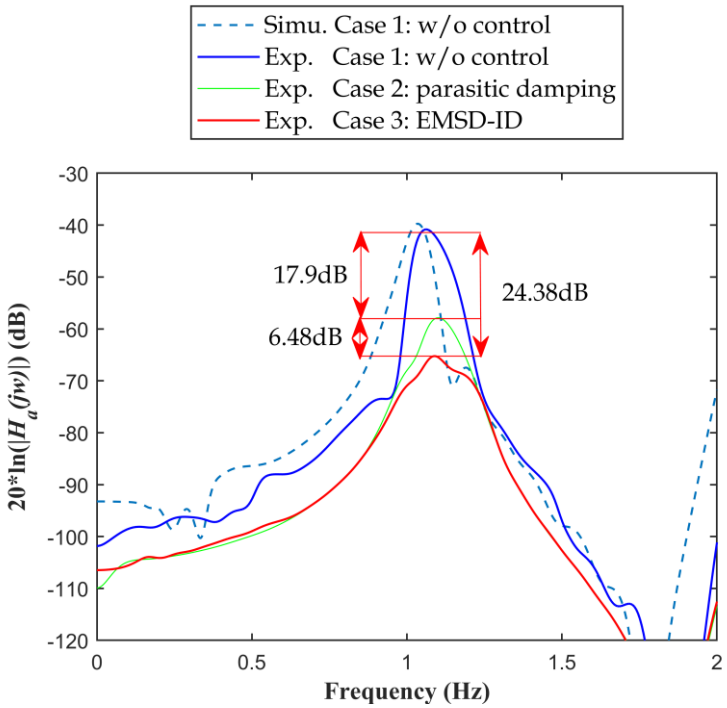


Fig. 17 (Color) FRF diagrams corresponding to the displacement responses at the 0.42L position.

The frequency response function (FRF) diagrams for Cases 1–3 were compared in Fig. 17. The FRF was calculated on the basis of the measured displacement responses at the 0.42*L* location and their corresponding input excitation forces. The FRF diagrams for Cases 2 and 3 were constructed on the basis of the responses obtained under sinusoidal sweeping excitation conditions, whereas those for Case 1 were constructed on the basis of the responses obtained under the random excitation condition with the frequency bandwidth of 0–5 Hz. The numerical results for Case 1 by adopting sweeping input signal were also included for cross-validation. The installation of the EMSD–ID (Case 3) reduced the first resonant peak by 24.38 dB in Case 3 relative to that in Case

1. Even comparing to Case 2 with parasitic damping, a 6.48 dB reduction was obtained through the installation of EMSD-ID.

## 6. Conclusions

The ability of the EMSD–ID to mitigate the vibration of cable-stayed bridges was experimentally and numerically investigated in this paper. Laboratory experiments were performed on a stay cable with a length of 135 m and installed with the newly designed and fabricated EMSD–ID. In addition to the discussion on experimental results, design concepts of EMSD–ID and the numerical simulations of the cable were also discussed. The major findings of this study are summarized as follows:

(1) The novel EMSD–ID, which emulates the mechanical behavior of traditional ID by employing an electromagnetic device connected to a capacitor-based shunt circuit and VNIC, was validated.

(2) The novel EMSD–ID could effectively enhance motor constants and provide large damping forces suitable for full-scale applications.

(3) The extremely high efficiency and flexibility of the EMSD–ID was illustrated by its ability to emulate an extensive range of inertance values. For example, the EMSD–ID could obtain an inertance of 12.3 t through the use of capacitors with a capacitance of 0.03 F weighting 660 g in the shunt circuit.

(4) The EMSD–ID yielded a damping ratio of 8% for the fundamental mode of the cable when installed at the 5% position of the stay cable. It is one of the highest damping ratios obtained in all the full-scale stay cable experiments so far.

## 7. Acknowledgement

The first three authors are grateful for the financial supports from the Research Grants Council of Hong Kong through a GRF grant (Project No.: PolyU 152222/14E)

and through a Research Impact Fund (Project No.: PolyU R5020-18), as well as from The Hong Kong Polytechnic University (Project No.: G-YBPZ). The fourth author acknowledges the National Natural Science Foundation of China (Grant No.: 51508217). The findings and opinions expressed in this paper are from the authors alone and are not necessarily the views of the sponsors.

**References**

Bloch, A. (1945). "Electromechanical analogies and their use for the analysis of mechanical and electromechanical systems." *Electrical Engineers - Part I: General, Journal of the Institution of*, 92(52), 157–169.

Cassidy, I. L., Scruggs, J. T., Behrens, S., and Gavin, H. P. (2011). "Design and experimental characterization of an electromagnetic transducer for large-scale vibratory energy harvesting applications." *J. Intell. Mater. Syst. Struct.*, 22(17), 2009–2024.

Chen, Z. Q., Wang, X. Y., Ko, J. M., Ni, Y. Q., Spencer, Jr., B. F., and Yang, G. (2003). "MR damping system on Dongting Lake cable-stayed bridge." In Proc., *Smart Structures and Materials 2003: Smart Systems and Nondestructive Evaluation for Civil Infrastructures*, edited by S.-C. Liu, 229. Bellingham, WA: International Society for Optics and Photonics.

Cheng, T. H., Wang, X. L., and Oh, I. K. (2009). "Electromagnetic multi-mode shunt damper for flexible beams based on current flowing circuit." In Vol. of 7493 Proc., 2nd Int. Conf. on Smart Materials and Nanotechnology in Engineering, 74930W-1–74930-8. Bellingham, WA: International Society for Optics and Photonics.

Hoang, N., Fujino, Y., and Warnitchai, P. (2008). “Optimal tuned mass damper for seismic applications and practical design formulas.” *Engineering Structures*, 30(3), 707–715.

Johnson, E. A. (2000). “Mitigating stay cable oscillation using semiactive damping.” *Proc. SPIE*, 3988(213), 207–216.

Johnson, E. A., Baker, G. A., Spencer, B. F., and Fujino, Y. (2007). “Semiactive Damping of Stay Cables.” *Journal of Engineering Mechanics*, American Society of Civil Engineers, 133(1), 1–11.

Johnson, E. A., Christenson, R. E., and Spencer Jr., B. F. (2003). “Semiactive Damping of Cables with Sag.” *Computer-Aided Civil and Infrastructure Engineering*, 18(2), 132–146.

Krenk, S. (2000). “Vibrations of a taut cable with an external damper.” *Journal of Applied Mechanics*, 67(4), 772–776.

Krenk, S., and Høgsberg, J. R. (2005). “Damping of cables by a transverse force.” *Journal of Engineering Mechanics*, 131(4), 340–348.

Lazar, I. F., Neild, S. A., and Wagg, D. J. (2016). “Vibration suppression of cables using tuned inerter dampers.” *Engineering Structures*, 122, 62–71.

Li, H., Liu, M., and Ou, J. (2008). “Negative stiffness characteristics of active and semi-active control systems for stay cables.” *Structural Control and Health Monitoring*, John Wiley & Sons, Ltd., 15(2), 120–142.

Li, H., Liu, M., Ou, J. P., and Guan, X. C. (2005). “Design and analysis of magnetorheological dampers with intelligent control systems for stay cables.” The rest of information.” *China Journal of Highway and Transport*, 18(4), 37–41.

Li, J.-Y., and Zhu, S. (2018). “Versatile Behaviors of Electromagnetic Shunt Damper

With a Negative Impedance Converter." *IEEE/ASME Transactions on Mechatronics*, IEEE, 23(3), 1415–1424.

Lu, L., Duan, Y.-F., Spencer, B. F., Lu, X., and Zhou, Y. (2017). "Inertial mass damper for mitigating cable vibration." *Structural Control and Health Monitoring*, e1986.

Main, J. A., and Jones, N. P. (2002). "Free vibrations of taut cable with attached damper. I: Linear viscous damper." *Journal Of Engineering Mechanics-Asce*, 128(10), 1062–1071.

Mehrabi, A. B., and Tabatabai, H. (1998). "Unified finite difference formulation for free vibration of cables." *J. Struct. Eng.*, 124(11), 1313–1322.

Meirovitch, L. (2001). *Fundamentals of Vibrations*. McGraw-Hil, New York.

Ni, Y. Q., Chen, Y., Ko, J. M., and Cao, D. Q. (2002a). "Neuro-control of cable vibration using semi-active magneto-rheological dampers." *Eng. Struct.*, 24(3), 295–307.

Ni, Y. Q., Ko, J. M., and Zheng, G. (2002b). "Dynamic Analysis of Large-Diameter Sagged Cables Taking Into Account Flexural Rigidity." *J. Sound Vib.*, 257(2), 301–319.

OVM Co. Ltd. (2014). "OVM GJ Prefabricated Strand Cable System with Integral Swaging Anchorage." http://kwansooweb.cafe24.com/wp-content/uploads/2016/02/Prefabricated-Strand-Cable.pdf .

Palomera-Arias, R. (2005). "Passive electromagnetic damping device for motion control of building structures." Ph.D Thesis, , Dept. of Architecture, Massachusetts Institute of Technology.

Shen, W., and Zhu, S. (2015). "Harvesting energy via electromagnetic damper: Application to bridge stay cables." *Journal of Intelligent Material Systems and*

*Structures*, 26(1), 3–19.

Shen, W., Zhu, S., and Xu, Y. (2012). "An experimental study on self-powered vibration control and monitoring system using electromagnetic TMD and wireless sensors." *Sensors Actuators A Phys.*, 180, 166–176.

Shi, X., and Zhu, S. (2015). "Magnetic negative stiffness dampers." *Smart Materials and Structures*, 24(7), 72002.

Shi, X., and Zhu, S. (2017). "Simulation and optimization of magnetic negative stiffness dampers." *Sensors and Actuators, A: Physical*, Elsevier B.V., 259, 14–33.

Shi, X., and Zhu, S. (2018). "Dynamic characteristics of stay cables with inerter dampers." *Journal of Sound and Vibration*, Elsevier Ltd, 423, 287–305.

Shi, X., Zhu, S., Li, J., and Spencer, Jr., B. F. (2016). "Dynamic behavior of stay cables with passive negative stiffness dampers." *Smart Materials and Structures*, IOP Publishing, 25(7), 1–14.

Shi, X., Zhu, S., and Nagarajaiah, S. (2017a). "Performance Comparison between Passive Negative-Stiffness Dampers and Active Control in Cable Vibration Mitigation." *Journal of Bridge Engineering*, 22(9), 1–15.

Shi, X., Zhu, S., and Spencer, B. F. (2017b). "Experimental Study on Passive Negative Stiffness Damper for Cable Vibration Mitigation." *Journal of Engineering Mechanics*, 143(9), 04017070.

Smith, M. C. (2002). "Synthesis of mechanical networks: the inerter." *IEEE Transactions on Automatic Control*, 47(10), 1648–1662.

Weber, F., and Boston, C. (2011). "Clipped viscous damping with negative stiffness for semi-active cable damping." *Smart Materials and Structures*, 20(4), 45007.

Wu, W. J., and Cai, C. S. (2007). "Theoretical exploration of a taut cable and a TMD

system.” *Engineering Structures*, 29(6), 962–972.

Xu, Y. L., and Yu, Z. (1998). “Mitigation of Three-dimensional Vibration of Inclined Sag Cable Using Discrete Oil Dampers - II. Application.” *Journal of Sound and Vibration*, 214(4), 659–673.

Zhou, H. J., and Sun, L. M. (2013). “Damping of stay cable with passive-on magnetorheological dampers: A full-scale test.” *International Journal of Civil Engineering*, 11(3), 154–159.

Zhu, S., Shen, W., and Xu, Y. (2012). “Linear electromagnetic devices for vibration damping and energy harvesting: Modeling and testing.” *Engineering Structures*, 34, 198–212.